Journal of Biomedical Optics

BiomedicalOptics.SPIEDigitalLibrary.org

Boundary discretization in the numerical simulation of light propagation in skin tissue: problem and strategy

Hao Jia
Bin Chen
Dong Li
Yong Zhang

SPIE.

Boundary discretization in the numerical simulation of light propagation in skin tissue: problem and strategy

Hao Jia, Bin Chen,* Dong Li, and Yong Zhang
Xi'an Jiaotong University, State Key Laboratory of Multiphase Flow in Power Engineering, Xi'an 710049, China

Abstract. To adapt the complex tissue structure, laser propagation in a two-layered skin model is simulated to compare voxel-based Monte Carlo (VMC) and tetrahedron-based MC (TMC) methods with a geometry-based MC (GMC) method. In GMC, the interface is mathematically defined without any discretization. GMC is the most accurate but is not applicable to complicated domains. The implementation of VMC is simple because of its structured voxels. However, unavoidable errors are expected because of the zigzag polygonal interface. Compared with GMC and VMC, TMC provides a balance between accuracy and flexibility by the tetrahedron cells. In the present TMC, the body-fitted tetrahedra are generated in different tissues. No interface tetrahedral cells exist, thereby avoiding the photon reflection error in the interface cells in VMC. By introducing a distance threshold, the error caused by confused optical parameters between neighboring cells when photons are incident along the cell boundary can be avoided. The results show that the energy deposition error by TMC in the interfacial region is one-tenth to one-fourth of that by VMC, yielding more accurate computations of photon reflection, refraction, and energy deposition. The results of multilayered and n-shaped vessels indicate that a laser with a 1064-nm wavelength should be introduced to clean deep-buried vessels. [DOI: 10.1117/1.JBO.20.2.025007]

Keywords: medical optics; light propagation; Monte Carlo method; tetrahedron mesh; skin tissues.

Paper 140842R received Dec. 17, 2014; accepted for publication Jan. 28, 2015; published online Feb. 24, 2015.

1 Introduction

Predicting light propagation in skin tissues is of theoretical importance to improve the clinical efficacy in the laser treatment of dermatosis, e.g., port wine stains (PWSs).[1] The Monte Carlo (MC) method is a versatile and easy-to-parallel approach[2] that has great potential in biomedical optics. In this method, features of a sizeable number of photon packets are collected to build the statistical behavior of light transportation.

Biological tissue is usually geometrically and constitutionally complicated in terms of computation. For instance, nonuniform energy distribution by selective photothermolysis is caused by various optical properties in different skin tissues, leading to preferential absorption in blood vessels rather than in other skin tissues including epidermis, dermis, and hair follicles.[3] Branched blood vessels and vessel clusters are also observed interspersing within the dermis through the reconstruction of PWS biopsy,[4] resulting in geometrical complexity and an unknown ending of light energy. Therefore, the effect of complicated heterogeneous adaptability has attracted considerable attention in the MC simulation. Wang et al.[5] show an ideal application of the MC method in multilayered tissues (MCML). In the original model, uniformed layers marked with different optical properties are stacked on top of each other and neighboring layers share a plain interface. Several studies[6,7] improved the MC method to adapt cylindrical surface boundaries (e.g., blood vessels) by employing Snell's law in the circular cross-section to trace the transport direction of light. This type of algorithm is referred to as geometrical MC (GMC) because the boundaries of adjacent objects (tissue structures) are defined geometrically and each object represents the biological constituents with the corresponding optical properties. However, GMC is rarely applied owing to an onerous mathematical description as it evolves to a more complicated situation.

With regard to light propagation in geometrically complex biological tissue, voxel-based MC (VMC) has attracted much attention.[8–10] In the VMC method, the model geometry is represented by a group of three-dimensional (3-D) stacked hexahedron voxels. VMC is widely investigated to explore photon radiation by assigning each hexahedron voxel certain optical properties, which include energy deposition and diffuse reflection, particularly in the simulation of laser treatment of PWS.[1,8] For laser wavelengths from 577 to 590 nm, a more uniformed energy distribution in the PWS vessel was reported when the wavelength increased. However, major errors (−80% to 120%) of photon intensity in boundary voxels are displayed when hexahedron faces are far from parallel to the axis planes.[11] However, the reason for these errors has not been clearly elucidated. Moreover, uneliminated errors exist even with finer discretization because inaccurate interfacial reflection and refraction do not disappear as the scale of voxels reduces.[7]

Compared with voxels, a tetrahedron mesh is ideally adaptable to an irregular interface. Shen and Wang[12] proposed a tetrahedron-based inhomogeneous MC optical simulator (TIM-OS) to balance the accuracy with flexibility. The computational results of TIM-OS agree well with those of MCML in single and multilayered tissues. However, the computational domains are mainly regular regions such as cuboids and multiple layers with less complexity. Providing a comprehensive description of

*Address all correspondence to: Bin Chen, E-mail: chenbin@mail.xjtu.edu.cn

1083-3668/2015/$25.00 © 2015 SPIE

mesh generation and photon transport of MC with tetrahedron grids in complex regions is necessary. To date, only a comparative study between mesh-based MC methods exists. Therefore, more studies are necessary to extend the TIM-OS method to laser propagation in complex skin models and to compare the precision between different mesh-based MC methods with the benchmark.

In the present paper, a tetrahedron-based MC (TMC) solver is developed. TMC is suitable for computing photon energy deposition in complicated domains with a body-fitted tetrahedron mesh. The applicability of TMC in a skin optics application is confirmed. The influence of discretization on the light propagation is discussed to compare the relative errors of VMC and TMC with the benchmark of GMC. Skin models with multilayered vessels and the curved vessel are investigated by TMC to indicate regulations of photon transport in complex tissue regions.

2 Methodology

From the viewpoint of geometrical optics, reflection and refraction on the interface occur when the photon packet hits a tissue boundary. When the incident angle and the normal direction are known, the reflection and refraction directions can be determined by reflection law and Snell's law. Figure 1 shows the universal interaction process. The normal vector **n**, incident vector **U**, reflection vector **V**, and refraction vector **W** are illustrated by solid arrows. The incident angle can be calculated as follows:

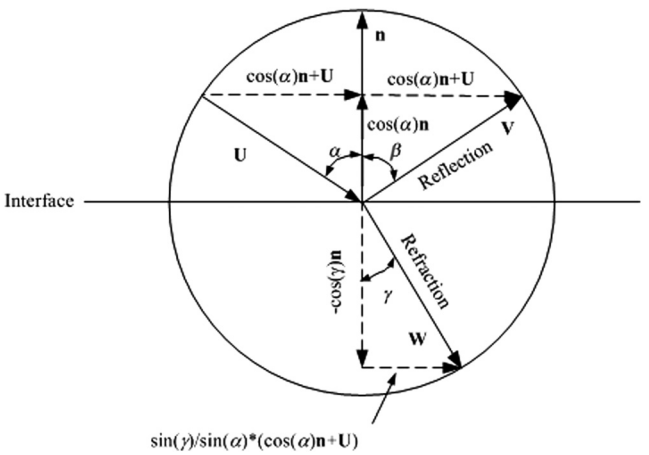

Fig. 1 Geometry for reflection and refraction.

$$\alpha = \arccos(-\mathbf{U} \cdot \mathbf{n}). \tag{1}$$

Reflection law states that the reflection angle equals the angle of incidence (Fig. 1) and is expressed as

$$\alpha = \beta. \tag{2}$$

If the photon is reflected, the reflection vector **V** can be calculated by

$$\mathbf{V} = \cos(\alpha) \cdot \mathbf{n} + [\cos(\alpha) \cdot \mathbf{n} + \mathbf{U}] = 2\cos(\alpha) \cdot \mathbf{n} + \mathbf{U}. \tag{3}$$

Snell's law indicates the relationship between the incident angle and the refractive angle when the refractive indices on both sides of the interface (n_α, n_γ) are given as

$$n_\alpha \cdot \sin\alpha = n_\gamma \cdot \sin\gamma. \tag{4}$$

Then the refraction direction can be written as

$$\mathbf{W} = -\cos(\gamma) \cdot \mathbf{n} + \sin(\gamma)/\sin(\alpha) * [\cos(\alpha) \cdot \mathbf{n} + \mathbf{U}]. \tag{5}$$

All the vectors in Fig. 1 are regarded as unit vectors, and the radius of the circle is a benchmark of these vectors' magnitudes.

In the bio-optics MC simulation, the direction of photon propagation is strongly related to the boundary shape. The normal vector used in the equations to obtain **W** and **V** is based on the interface description. For GMC, VMC, and TMC algorithms, the discretization of a curved boundary is quite different. Figure 2 displays the different discretizations and photon reflections on a circular boundary. As shown in Fig. 2(a), GMC gives a nondiscretized, analytically defined geometry. Grid and discretization are unnecessary, and the photon motion is determined by the reflection of the incident vector on the interface. For this case, the circular shape of a cylinder can be easily described mathematically, but more complex conditions make GMC difficult to implement.

In contrast, VMC and TMC are both grid-based methods. In VMC, the computational domain is represented by a 3-D matrix of hexahedron voxels [Fig. 2(b)]. The interface (material boundary) may cross several grid cells, resulting in so called interface cells. Boundary distortion caused by interface cells may greatly deviate from the real direction of reflection and refraction, because the approximated zigzag interface is only parallel to the three coordinate axes [Fig. 2(b)]. Another issue is the error caused by the optical properties in such cells. During computation, optical properties related to certain tissues (e.g., epidermis,

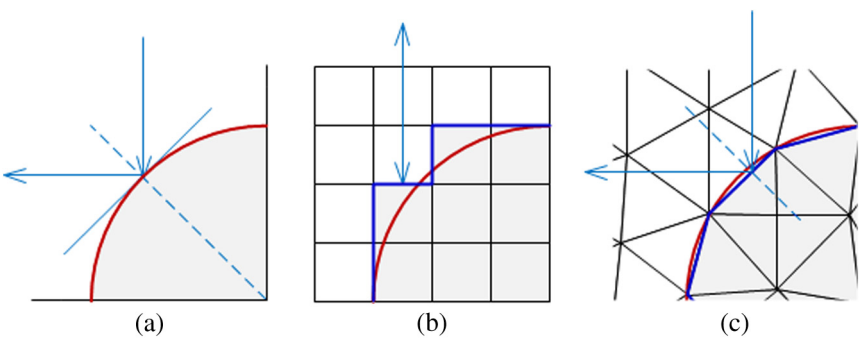

Fig. 2 Photon reflection on vessel-dermis boundary: (a) geometry-based Monte Carlo (GMC), (b) voxel-based MC (VMC), and (c) tetrahedron-based MC (TMC).

dermis, and blood) are assumed uniform in such cells for convenience. However, the cell interface is composed of different tissues. Large differences in optical properties (especially the refractive index) between the two sides of the interface indicate the occurrence of larger errors.

Unstructured mesh is a promising solution. TIM-OS[12] is used in the preliminary attempt. However, it is an incomplete solution to the interface mesh problem in VMC. In TIM-OS, a computational domain is separated into several equal cuboids which are then divided into six tetrahedra. In this way, a tetrahedron-based finite-element mesh is obtained. Apparently, the interface tetrahedra still exist and the discretization problem in VMC is not solved.

The real solution is the body-fitted TMC, where the curved boundary is approximated by a mesh of irregular tetrahedra. The tetrahedra are generated along the interface, yielding a polyhedron approximation to match the real interface [Fig. 2(c)]. Compared with GMC, TMC can adapt more complex interfaces. No interface cells exist in TMC, hence avoiding the discretization problems rising in VMC and TIM-OS. Moreover, the photon in TMC will intersect with one of the four triangular faces instead of the six rectangles in VMC when it travels from one body cell to another. Such a difference provides TMC more flexibility and accuracy in treating the photon-boundary interaction, resulting in fewer artificial errors. When a neighbor tetrahedron has a different refractive index, the photon with the known propagation direction can be reflected or transmitted to any direction. In the VMC method, only three options exist because the boundary face shaped by a rectangle only has three normal directions.

In mesh-based MC, another problem occurs when the photon incidents along the edge or corner of a grid cell. The direction vector in such position is called a "critical vector," as shown in Fig. 3 for VMC, TIM-OS, and TMC. Determining a tissue type in the forward direction of the photon with a critical vector is difficult because the photon may continue to transport very close to the cell boundary, which may lead to computational failure. When the photon intersects with hexahedra (GMC) or finite element grids (TIM-OS), the critical vector is limited because of the simple mesh organization [blue arrows shown in Figs. 3(a) and 3(b)].

In TMC, the body-fitted mesh is generated across the interface. The intricacy connection of the mesh in TMC (blue arrows shown in Fig. 3(c) results in increasing critical vectors. Thus, TMC can improve the adaptability in complex regions and enhance the possibility of photon propagation along the critical direction. To solve the problem of optical property confusion of different tissues between neighboring cells, we defined a minimum threshold δ as the minimum distance from the photon-cell intersection to the boundary of neighboring cells (as shown in Fig. 4). The δ can be set as 10^{-8} to 10^{-10} of the mesh interval. If

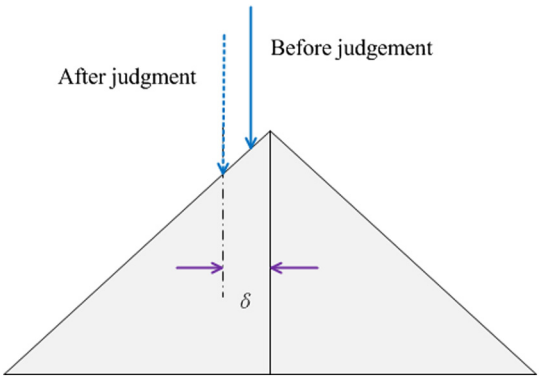

Fig. 4 Threshold of the distance.

the distance from the intersection point to the cell boundary between different cells (tissues) is less than δ, then the photon is located in the serious region. Optical parameters are confused if the photon continues to propogate exactly close to the cell boundary. To avoid such a case, we can shift the incident position of the photon parallel to δ.

In the present study, energy deposition and diffuse reflection fluence of the laser propagation in the treatment of PWS are investigated to compare the VMC and TMC algorithms with GMC as a benchmark. In PWS patients, blood vessels of an average buried depth of 0.46 mm[13] progressively become ecstatic with age, giving the skin a pink to purple color. The laser treatment is based on selective photothermolysis[13] by preferential absorption of laser light by using the erythrocytes in blood. Certain laser systems are explored to heat up the dilated blood vessels. If a critical temperature field (70°C)[13] is maintained long enough above the vessels, irreversible injury occurs to the blood lesions. Nevertheless, the absorption of laser energy by melanin in the epidermis should be avoided to protect the skin surface from thermal damage.

Figure 5 illustrates a 3-D two-layered skin model representing a cuboid epidermis and a much thicker dermis. A blood vessel buried in the dermis is represented by a horizontal cylinder parallel to the skin surface. The dermis-vessel interface is used as an example to compare the implementation of the three MC methods. This simplified model is widely adopted in the MC computation for optical skin interaction.[1,7,8]

For tracing photons in skin tissue with epidermis, dermis, and vessels by the MC simulation, each incident photon packet with an initial weight propagates and attenuates through the different layers. The energy deposition rate in the light attenuation is determined by absorption and scattering effect controlled by the local tissue optical properties. The implementation of MC simulation is demonstrated in detail by Wang et al.[5] When the photon packet hits a boundary, the reflection

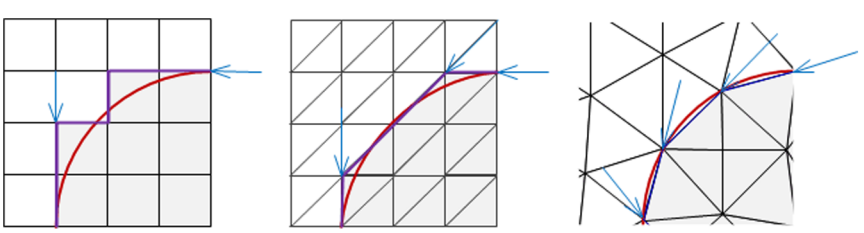

Fig. 3 Critical directions of photons at the interface: (a) GMC, (b) VMC, and (c) TMC.

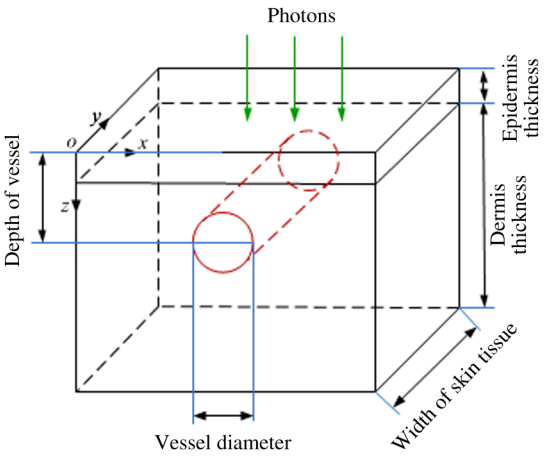

Fig. 5 Diagram of skin model.

and transmittance behaviors at the interface are analyzed. If a photon escapes from the computational domain or drops its weight to zero, it will be removed from the computational list. Considering the specular reflectance (E_{sp}) as the entrance limitation of a photon packet,[5] the total energy balance is given as follows:

$$E = E_{re} + E_{trans} + E_{side} + E_v + E_d + E_e + E_{sp}, \quad (6)$$

where E_{re}, E_{trans}, and E_{side} are the escaped energies from the top surface, bottom surface, and four sides of the computational domain, respectively. E_v, E_d, and E_e are the absorbed energies by the vessel, dermis, and epidermis, respectively.

Table 1 Parameters for the two simulations.

Simulation	Domain	μ_a (cm^{-1})	μ_s (cm^{-1})	g	n	Cell number
Case 1	10 mm × 10 mm × 0.5 mm	0.5	800	0.9	1.46	2978
Case 2	10 mm × 10 mm × 1 mm	4.0	3200	0.9	1.46	784

3 Validation of the Tetrahedron-Based Monte Carlo Method

To validate the TMC algorithm, we initially compared TMC with GMC by recording the diffuse reflectance fluence in a single-layered slab with thicknesses of 0.5 and 1 mm. A total of 10 million photons were launched at the position (0, 0, 0) in the direction (0, 0, 1) in the following two cases. The size of the transverse dimension is limited to 10 mm × 10 mm because almost no photon weight exists (actually less than 0.01% of the total weight) or is added to the fluence when enlarging the cross section. In the TMC method, the tetrahedron mesh is generated by commercial software GAMBIT 2.4. The body-fitted tetrahedra are generated along the vessel-tissue interface (vessel wall), which is efficient in increasing the accuracy because no interface tetrahedra exist. Optical properties[12] and cell numbers in TMC are presented in Table 1. Different cell numbers are used for the two cases to check the accuracy of TMC over one layer of mesh, i.e., a mesh interval is set as the tissue thickness.

In the simulation, fluence is recorded with respect to the distance to the center of the incident plane using a group of annular regions. The width of the ring is 0.01 mm. Figure 6 compares the diffuse reflectance fluence among GMC, TMC, and TIM-OS[12] in the two numerical experiments. In TIM-OS, the slab is initially partitioned into a set of 0.5 mm cubes for case 1. Each cube is broken down into six tetrahedra, and a finite element mesh with 2400 tetrahedra is obtained. For layers of 1-mm thickness, a set of 1 mm cubes is applied, leading to 600 tetrahedra. As shown in Fig. 6, the results computed by TMC and TIM-OS are consistent with that by GMC, confirming the validation of the TMC algorithm. A little more consistent results of fluence by TIM-OS is noted in case 1 between 0.03 and 0.15 mm, but generating tetrahedra by TIM-OS leads to interface cells. If TIM-OS and TMC are both implemented in a more complicated domain with curved boundaries, more accurate results can be expected from TMC because of the body-fitted grids.

4 Influence of the Boundary Discritization

GMC, VMC, and TMC algorithms are compared by simulating the two-layer skin model (Fig. 5), representing the epidermis (thickness: 60 μm) and dermis (940 μm) underneath. A 1.4 mm × 1.4 mm × 1.0 mm domain is used because it is sufficiently large and no evident fluence variation occurs across the tissue boundary. A uniform mesh with the spatial discretization

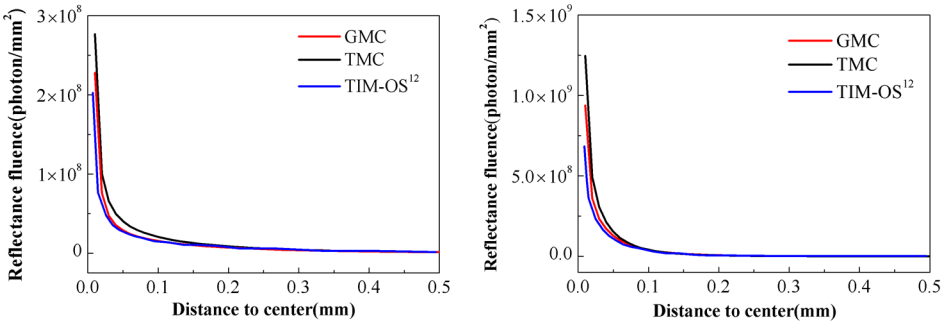

Fig. 6 Comparison of diffuse reflectance fluence profiles between TMC and GMC: (a) Case 1, and (b) Case 2.

step of $\Delta x = \Delta y = \Delta z = 5$ μm is implemented in VMC, and $280 \times 280 \times 200 = 1.6 \times 10^7$ cells (with 1.27×10^5 cells in the blood vessel region) are adopted. The same uniform mesh is used as a background mesh in GMC to count the energy deposition. In the TMC method, the mesh is generated on the three zones (epidermis, dermis, and blood vessel) by GAMBIT software. Adjacent zones share the same face mesh. Given the high absorption in the epidermis and blood vessels, local refinement is implemented in these two regions. Spatial discretization steps are 10, 50, and 10 μm in the epidermis, dermis, and blood vessel, respectively. The cell number is about 1.54×10^6, among which 1.24×10^5 is a mesh in the vessel region. In this way, the three methods share almost the same mesh density in the vascular region, providing a convenient way to compare the different algorithms.

Optical properties corresponding to the wavelength of 585 nm are presented in Table 2. The laser beam assumed a flat top profile with a fluence of 1 J/cm^2 and a diameter of 1.0 mm, centered at $x = 700$ μm, $y = 700$ μm, and $z = 0$ μm.

4.1 *Skin Tissue Reply to Photon Energy*

We consider a single horizontal blood vessel in the dermis with a diameter of 120 μm, centered at a depth of 250 μm under the skin surface. Table 3 presents the diffuse reflectance, deposition, and escape of photon energy based on Eq. (6). The results by VMC and TMC are consistent with GMC.

The total escape energy is about 45%, of which 16% overflows from the top surface. This energy loss should be controlled in a laser therapy application. The volume ratio of the dermis is larger than that of the epidermis and vessels. Thus, absorption by dermis is lower than that by the epidermis and larger than that by the vessels, although the absorption rate for a 585-nm laser is low in the dermis.

Table 4 illustrates the energy absorptivity of each skin tissue and the energy escape from each boundary, as well as the statistical results of movement and energy attenuation of abundant photons. The energy deposition rate is highest within the vessel, much weaker in the epidermis, and almost negligible in the dermis. The data confirm that about 17.8% of dermis absorption in Table 3 is mainly caused by the large volume. From the viewpoint of escape, the top surface takes the largest proportion, showing frequent photon activity. The total deposited energy in each tissue shows little information across the tissue boundary; thus, investigating the deposition distribution on the tissue boundary is necessary.

Table 2 Tissue optical parameters for 585 nm.[8]

Tissue	μ_a (cm^{-1})	μ_s (cm^{-1})	g	n
Epidermis	18	470	0.790	1.37
Dermis	2.2	129	0.790	1.37
Blood	191	468	0.995	1.33

Table 4 Efficiency rate of skin tissues to photon energy.

Skin tissue	Absorption ratio (unit volume)	Boundary	Escape ratio (unit area)
Epidermis : dermis	21 : 1	Top : side : bottom	8 : 4 : 3
Blood : dermis	78 : 1		

4.2 *Deposition Error Analysis on the Tissue Boundary*

4.2.1 *Vessel paralleled to coordinate axis*

We consider a single horizontal blood vessel in the dermis with a diameter of 120 μm, centered at a depth of 250 μm under the skin surface. The vessel is parallel to the y-axis in Fig. 2. For the VMC method, such a configuration indicates that the blood-dermis interface mesh only exists in the x-z plane, yielding the least distinction between VMC and TMC. The photon deposition distribution in the cross section of the vessel is shown in Fig. 7. The top half of the vessel, which faces the photon initial direction, collects more energy than the bottom half. The results of TMC agree well with those of GMC, whereas an apparent zigzag appears across the vessel boundary with VMC. This finding is attributed to the existence of interface cells in the structured mesh, leading to reflection error and inaccurate optical properties, which cannot help VMC to adapt to complex boundary shapes.

Deposition errors close to the boundary are collected in certain zones for a quantitative analysis. In the axial cross section of the vessel shown in Fig. 8(a), a group of annular rings with a thickness of 1 μm close to both sides of the vascular wall (red circle) is selected as the error analysis region. The black arrow represents the initial direction of photons. The horizontal line, which passes through the vessel center, parts the circular rings into two groups: a light side and backlight side. To further study the circumferential distribution of energy deposition, we segmented the 5-μm thickness annulus close to the inner vascular wall into 360 parts [see Fig. 8(b)]. Each 1-deg annulus is one statistical unit.

Table 3 Photon ending.

585 nm	E_{sp} (%)	E_e (%)	E_d (%)	E_v (%)	$E_e + E_d + E_v$ (%)	E_{re} (%)	E_{side} (%)	E_{trans} (%)	$E_{re} + E_{side} + E_{trans}$ (%)
Geometry-based Monte Carlo (GMC)	2.4	23.5	17.2	11.6	52.3	16.0	22.9	6.4	45.3
Voxel-based MC (VMC)	2.4	22.8	17.8	11.9	52.5	17.4	19.6	8.1	45.1
Tetrahedron-based MC (TMC)	2.4	22.8	17.8	11.8	52.4	17.4	19.7	8.1	45.2

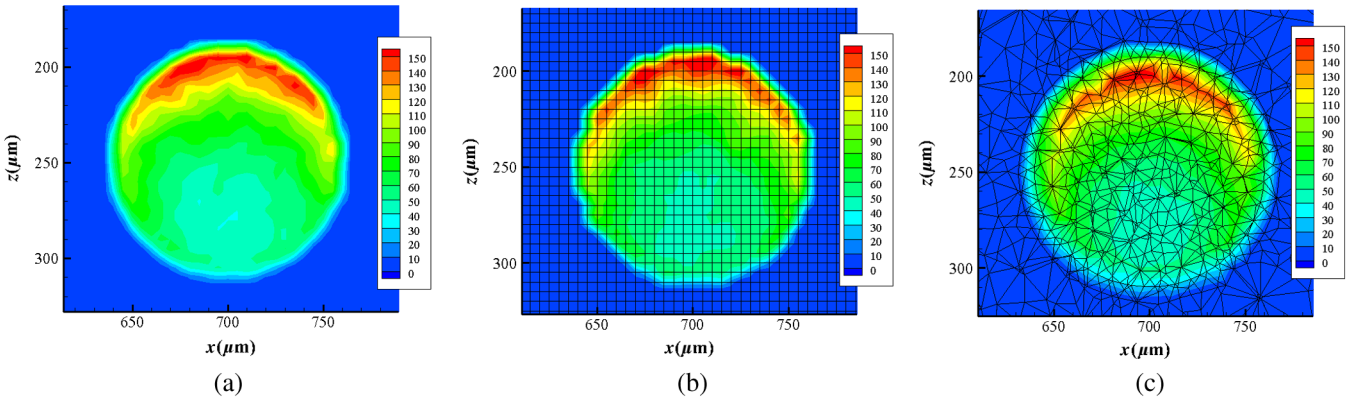

Fig. 7 Photon deposition in the cross section in the vascular region: (a) GMC, (b) VMC, and (c) TMC.

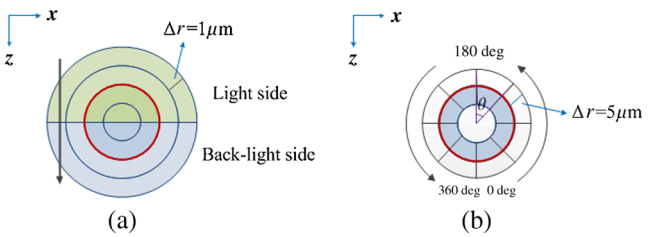

Fig. 8 Statistical area of error analysis: (a) half-annular region of the vascular wall, and (b) axial region of the vascular wall.

With GMC as a benchmark, the deposition in the half-annulus area computed by GMC, VMC, and TMC is collected. The relative error K_T (or K_V) of VMC (or TMC) is calculated as follows:

$$K_T = \frac{E_T - E_G}{E_G}, \qquad K_V = \frac{E_V - E_G}{E_G}, \tag{7}$$

where E is the photon deposition in each half annulus.

Figure 9 depicts the deposited energy and its error in the half-annulus region. The horizontal direction shows the distances between the outside of each annulus and the vessel center. Negative and positive values represent the light and backlight sides, respectively. From the energy deposition [Fig. 9(a)], the result by TMC is associated with that by GMC. In VMC, however, the error on the interface (± 5 μm at -60 and 60 μm) has a great deviation from GMC and fluctuates critically. Figure 9(b) shows that the maximum relative errors of VMC are -35% in the light side and -20% in the backlight side, whereas the errors of TMC decrease to about one fourth of that value (-8% and -5%, respectively).

Figure 10 compares the energy depositions in half-annulus regions at vessel depths $z = 375$ and 500 mm. In Fig. 8 ($z = 250$ mm), the deep vessel leads to an increase in the absorption peak on the vascular wall. The errors of VMC and TMC at the vessel boundary at different vessel depths show similar behaviors. The error of TMV is also consistent with that of VMC in the vessel region (-55 to 55 μm). The errors of TMC and VMC are all higher than that of GMC. These errors are uniformly distributed and slightly increase with depth. These results are due to the deposition in deep vessels, which is mainly derived from scattered light. The photon energy is absorbed by a deep vessel after an intersection with more grid cells, leading to a more apparent fluctuation of energy deposition by mesh discritization.

Figure 11 presents the energy deposition and relative error distribution of a 1-deg annulus. As shown in Fig. 11(a), energy deposition obtained by GMC exhibits a normal distribution along the circumferential direction. This normal distribution is reasonable because the energy absorption at the top of the vessel (180 deg) is the highest, whereas that at the bottom of the vessel (0 deg) is the lowest. The results by TMC agree well with those by GMC. However, a significant minus deviation in VMC can be observed at 20 deg to 70 deg and 110 deg to

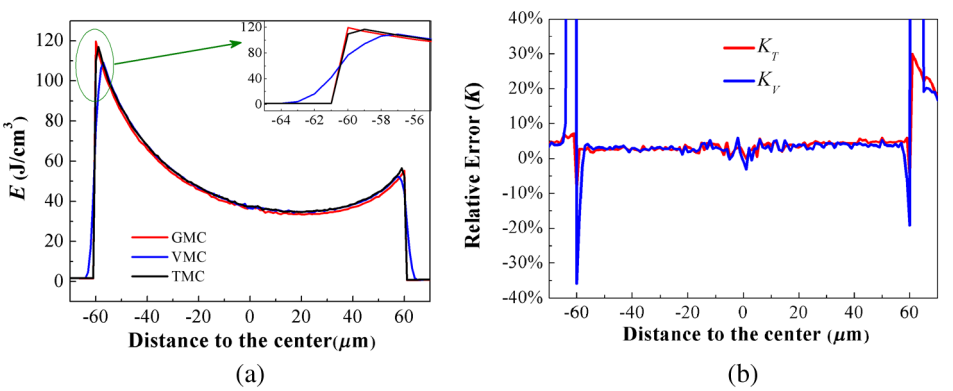

Fig. 9 Photon deposition and error distribution in half-annular regions: (a) energy deposition, and (b) relative error.

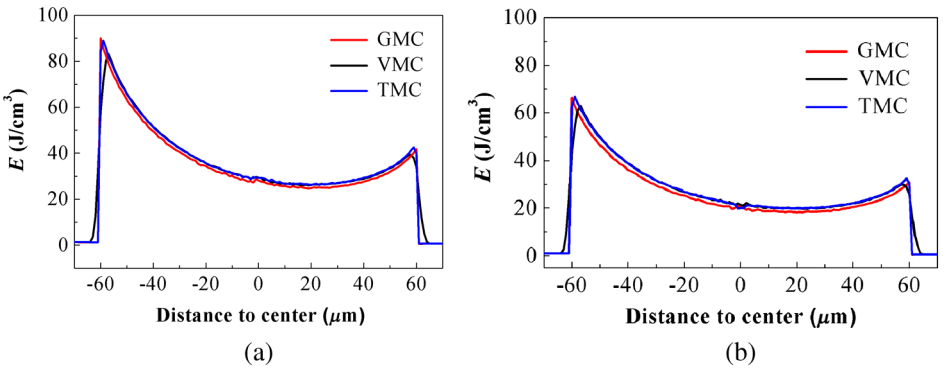

Fig. 10 Photon deposition at different depths: (a) $z = 375$ mm, and (b) $z = 500$ mm.

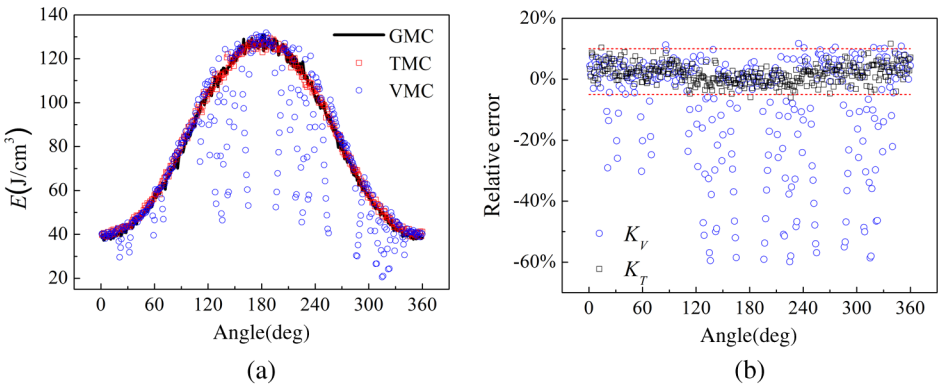

Fig. 11 Energy deposition and relative error distribution in 1-deg annulus region: (a) energy deposition, and (b) relative error.

170 deg away from the positive z direction. Figure 8(b) clearly shows that K_V is widely scattered and may fluctuate to -60%, whereas K_T is maintained in a small range from -5% to 10% (between the red dashed lines). In several angle ranges, K_V is 10 times larger than K_T. In contrast to K_T, K_V is highly sensitive to different angles. Figure 12 compares the deposition at vessel depths $z = 375$ and 500 mm. Absorption peak decreases with vessel depth.

In VMC, changes of the vessel radius lead to different numbers of interface cells, yielding different errors. To investigate the influence of vessel diameter, we used 60, 120, and 180 μm to compute the average energy deposition in each 1-deg annulus:

$$R_T = \frac{1}{360}\sum_{i=1}^{360}\frac{\langle E_{\mathrm{ang},i}\rangle_T - \langle E_{\mathrm{ang},i}\rangle_G}{\langle E_{\mathrm{ang},i}\rangle_G},$$
$$R_V = \frac{1}{360}\sum_{i=1}^{360}\frac{\langle E_{\mathrm{ang},i}\rangle_V - \langle E_{\mathrm{ang},i}\rangle_G}{\langle E_{\mathrm{ang},i}\rangle_G}, \tag{8}$$

where $E_{\mathrm{ang},i}$ is the deposited energy in the region within the i'th annulus. R_T and R_V are the average errors of deposited energy. Table 5 shows that R_V is four to six times larger than R_T. Although vessels with larger diameters have a relatively smooth interface, R_V and R_T do not decrease with vessel diameter. R_T is insensitive to vessel diameter.

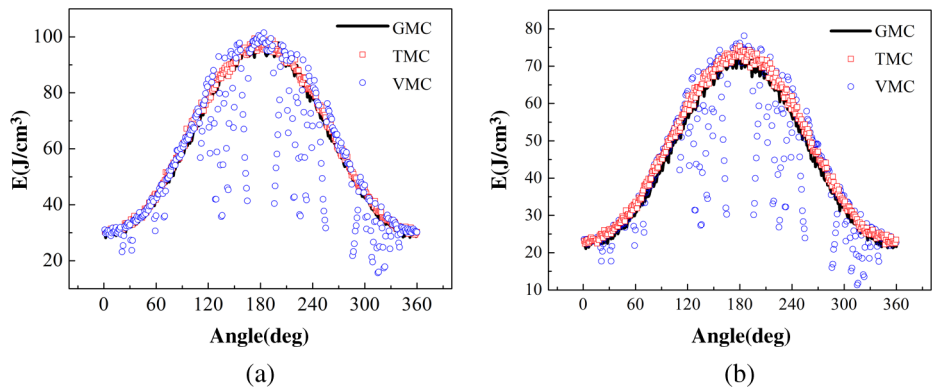

Fig. 12 Photon deposition in axial region: (a) $z = 375$ mm, and (b) $z = 500$ mm.

Table 5 Influence of deposition error by blood vessel diameter.

Vessel diameter d (μm)	R_T (%)	R_V (%)
60	−1.08	−5.74
120	1.75	−6.96
180	1.04	6.58

4.2.2 *Inclined vessel*

If the vessel is rotated on a horizontal plane, more interface cells are generated in the VMC method. Larger errors are expected to occur with the VMC method compared with the TMC method. Figures 13(a) and 13(b) represent the vessel positions before and after rotation, respectively. The vessel axes are $x = 700$ μm and $x = y$.

Given that the laser spot is in the center of the incident plane and the relative location between the spot and the vessel is not changed before and after rotation, the photon energy distribution in the vessel should remain intact. The relative error after rotation is defined as follows:

$$Q = \frac{1}{360}\sum_{i=1}^{360}\frac{\langle E_{\text{ang}}\rangle_{\text{rot}} - \langle E_{\text{ang}}\rangle_{ori}}{\langle E_{\text{ang}}\rangle_{\text{ori}}}, \tag{9}$$

where $\langle E_{\text{ang},i}\rangle_{\text{ori}}$ and $\langle E_{\text{ang},i}\rangle_{\text{rot}}$ are the photon depositions in each 1-deg annulus region before and after rotation, respectively. The results show that Q_V (4.08%) is larger than Q_T (0.09%), indicating that the spatial adaptability of TMC is superior to that of VMC.

Figure 14 compares the relative error of energy deposition before and after rotation. Rotation yields more K_V data with a large error (more than −5% to 10%, between two red dashed lines). These data scatter to all angles instead of concentrating in a certain angle area. Table 6 presents the energy distribution over the region. Only two or three data of K_T are found outside the region regardless of rotation, representing less than 1% of all points. With regard to K_V, 40 new data are added to the external region, representing 34.2% to 54.7% of all points. More than half of the data overflow out of the region, which greatly influences the computational precision. TMC shows better

Table 6 Energy deposition error distribution in the region before and after rotation.

Region: −5% < K < 10%	K_T		K_V	
	Before	After	Before	After
Data points in the region	357	358	237	197
Data points out of the region	3 (0.83%)	2 (0.56%)	123 (34.2%)	163 (54.7%)

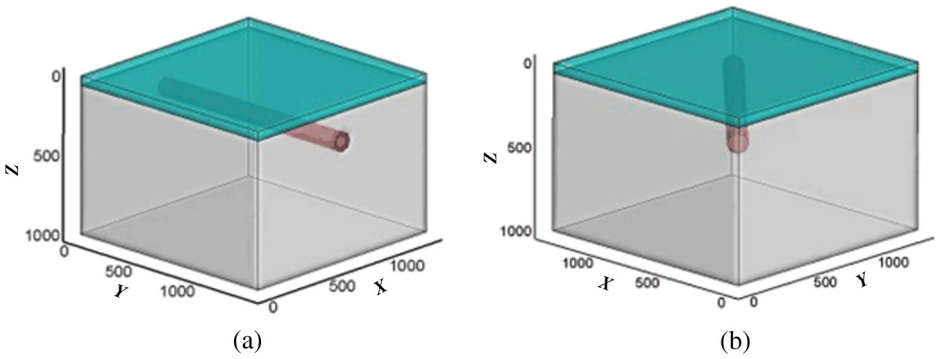

Fig. 13 Blood vessel rotation in x-y plane: (a) before rotation, and (b) after rotation.

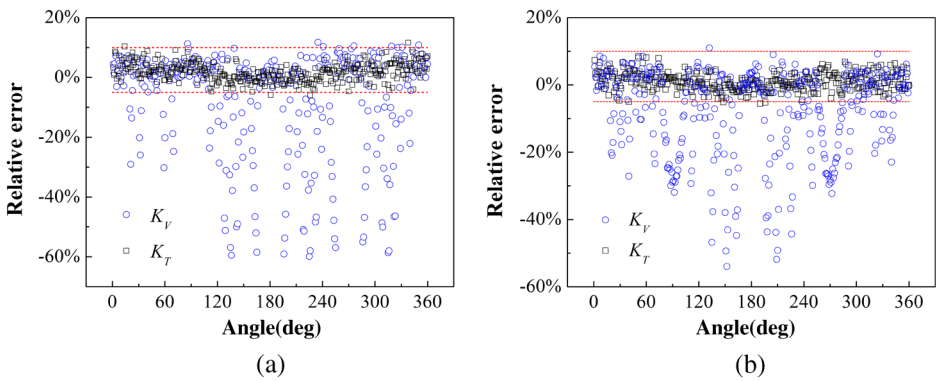

Fig. 14 Error distribution of energy deposition by vessel rotation: (a) before rotation, and (b) after rotation.

results than VMC because the latter generates more interface cells after rotation.

4.3 *Laser Propagation in More Complicated Skin Model by Tetrahedron-Based Monte Carlo Method*

The above simulations verify that the error of TMC is much less than that of VMC. Thus, TMC is an appropriate candidate to investigate a more complex skin model. Energy depositions in skin with irregular vessels, including multilayered and cured vessels, are investigated by TMC.

4.3.1 *Multilayered vessels*

A skin model that involves two cylindrical blood vessels is displayed in Fig. 15(a). The parameters of the two vessels are all the same except for the depth. Figures 15(b) and 15(c) illustrate the contour of energy deposition in the cross-section and energy deposition in the depth direction at the beam center. An apparent shading effect can be observed because of the absorption of the superficial vessel. The peak absorption value of the deep-seated vessel is 60 J/cm^3, which is far below the superficial layer vessel (140 J/cm^3). Thus, the deeper vessel receives insufficient thermal damage.

A multilayered vessel model is used to further investigate the shading effect. Figure 16(a) shows the geometry model of three-layered vessels. Vessel count increases with layers. As shown in the two-dimensional (2-D) deposited energy profile [Fig. 16(b)], vessel absorption deceases progressively with each layer. Compared with the deeper layer in Fig. 15, absorption by vessels in the second layer is higher in Fig. 16(b) because of the less direct shade to the initial photon direction.

The symmetry axis of absorption is unparallel to the z-axis in the side vessel in the last two layers. Instead, it turns an angle toward the spot center. The more a vessel location is deviated from the center indicates the more the symmetry axis is deviated. This result is due to the fact that in the vascular wall, the asymmetry of a photon's collision along the wall circumference becomes stronger as the location of the vessel is farther from the spot center. In the third layer, asymmetry also leads to more deposition in the middle vessel than its two sides even with the shade by the first layer.

Figure 16(c) presents the energy deposition versus depth at the beam center. As the vessel layer and number increase, the vessels in the deepest layer only receive less photon energy, even smaller than that in the epidermis. This result implies that the laser with a 585-nm wavelength has a limited penetration depth and is difficult to cause damage to the lesion hidden in the deep layers.

4.3.2 *Curved vessel*

An n-shaped curved vessel model [Fig. 17(a)] is shown in Fig. 17(b). Energy mainly deposits at the vessel top. The two "arms" of the n-shaped vessel absorb less energy because of these two factors: direction and depth. The direction of the "arm" part is perpendicular to the photon incident plane; thus, the deposition is mainly due to scattered light which has a

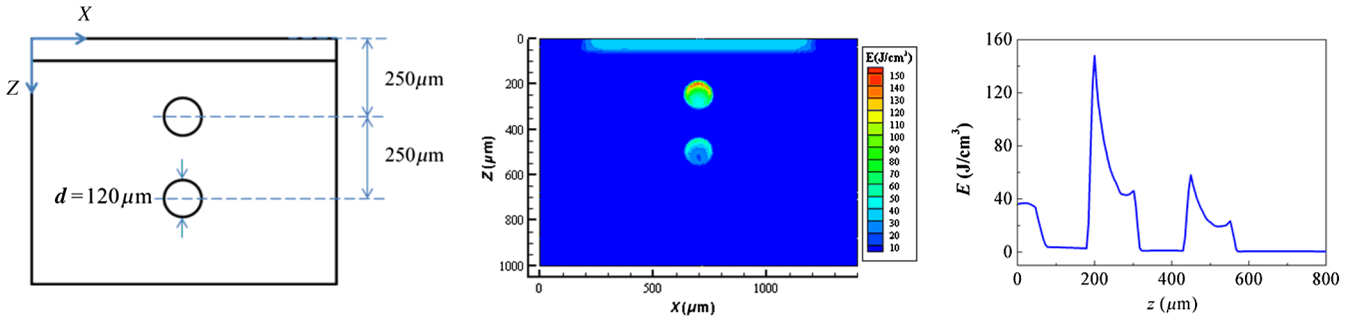

Fig. 15 Two vessels: (a) geometry model, (b) two-dimensional (2-D) deposited distribution, and (c) deposition versus depth at beam center.

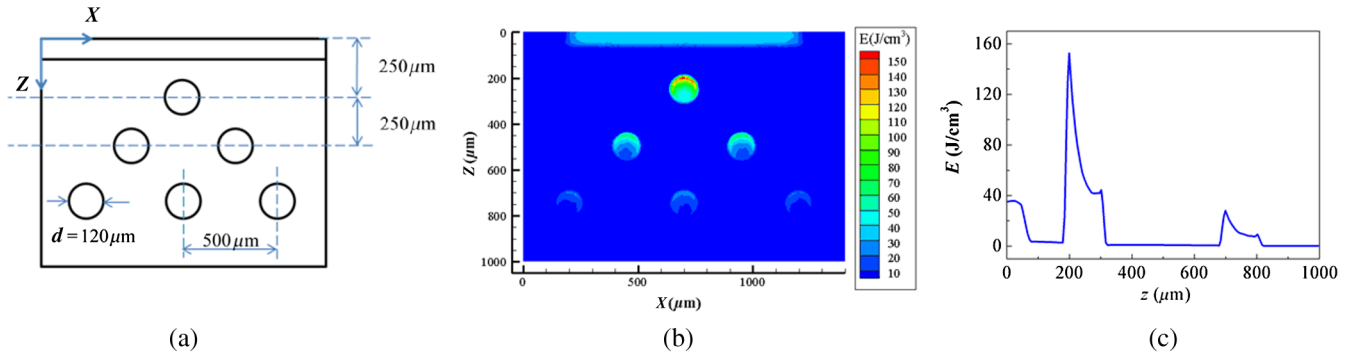

Fig. 16 Multilayered vessels: (a) geometry model, (b) 2-D deposited distribution, and (c) deposition versus depth at beam center.

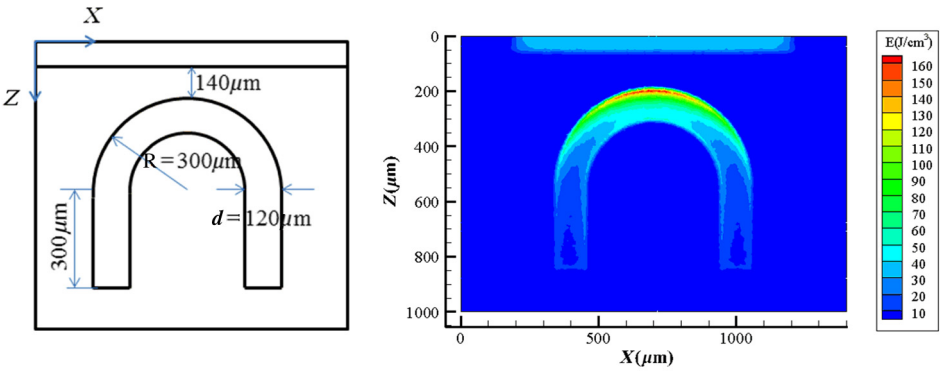

Fig. 17 Curved vessel: (a) geometry model, and (b) energy deposition.

stronger penetration depth. In addition, with the increasing depth, the dermis absorbs and scatters some energy and decreases the radiation energy to deeper vessels. The wavelength adopted in this work is 585 nm, which has insufficient penetration depth. For the treatment of a deep-buried vessel, combining the existing laser with strong penetration depth (e.g., Nd:YAG laser with a wavelength of 1064 nm) may be considered to achieve the thermal damage of the vertical vessel in the deep layer.

5 Conclusion

Among all the factors that influence the MC simulation of light propagation in biotissue, spatial discretization is of considerable importance. The VMC method has a significant error compared with nondiscretized GMC because the curved interface cannot be approximated well with a zigzag polygonal shape. To solve this problem, we developed a TMC method in this work. Body-fitted tetrahedra are generated in different tissues. No interface tetrahedral cells exist, thereby avoiding the error of photon reflection in the interface cells in VMC. By introducing the distance threshold, the error caused by confused optical parameters between neighboring cells when photons are incident along the cell boundary can be avoided. In comparison, the TMC method combines partition grid generation with a local refinement technique to approximate the real curved boundary well.

Slices by 3-D image of the photon energy distribution show that a more smooth interface can be captured by TMC than VMC. To compare the precision in the vessel-dermis boundary by VMC and TMC algorithms, we selected light propagation in the half-annulus regions close to the vascular wall as analysis zones. In the inner part of the vascular wall, the maximum relative error of VMC is −35% in the light side and −20% in the backlight side, whereas that of TMC is −8% and −5%, respectively. In the 1-deg annulus regions of the vascular internal wall, the deviation reaches to −60% in VMC, whereas the deviation in TMC is maintained in a narrow range from −5% to 10%. The VMC method is very sensitive to vessel rotation because of more interface cells. Vessel rotation leads to an evident rise of large error data points (from 34.2% to 54.7%). TMC has better spatial adaptability, and the proportion is from 0.83% to 0.56%, with neglected changes. The shading effect caused by multilayered and curved vessels has a prominent influence on the distribution of deposited energy. A long wavelength laser (near-infrared) should be incorporated to cause damage to the deeper buried vessels.

The tetrahedron mesh applied in the MC program can improve the smoothness of the tissue interface shape and avoid an artificial serrated polygonal boundary. This effect would be more apparent when the error in each boundary cell is compared against the statistics of the whole vessel. Thus, TMC is superior to VMC with a better approximation of the curved boundary, yielding more accurate computation of photon reflection, refraction, and energy deposition.

Acknowledgments

This work was supported in part by the National Natural Science Foundation of China (51336006), the International Science & Technology Cooperation Plan of Shaanxi Province (2013KW30-05), and the Fundamental Research Funds for the Central Universities.

References

1. G. W. Lucassen et al., "Light distributions in a port wine stain model containing multiple cylindrical and curved blood vessels," *Lasers Surg. Med.* **18**, 345–357 (1996).
2. Q. Fang, "Mesh-based Monte Carlo method using fast ray-tracing in Plücker coordinates," *Biomed. Opt. Express* **1**(1), 165–175 (2010).
3. R. R. Anderson and J. A. Parrish, "Microvasculature can be selectively damaged using dye lasers: a basic theory and experimental evidence in human skin," *Lasers Surg. Med.* **1**, 263–276 (1981).
4. T. J. Pfefer, J. K. Barton, and D. J. Smithies, "Modeling laser treatment of port wine stains with a computer-reconstructed biopsy," *Lasers Surg. Med.* **24**, 151–166 (1999).
5. L. Wang, S. L. Jacques, and L. Zheng, "MCML—Monte Carlo modeling of light transport in multi-layered tissues," *Comp. Methods Prog. Biomed.* **47**(2), 131–146 (1995).
6. J. Zhou and J. Liu, "Numerical study on 3-D light and heat transport in biological tissues embedded with large blood vessels during laser-induced thermotherapy," *Numer. Heat Tranfser, Part A* **45**, 415–449 (2004).
7. J. Premru, M. Milanič, and B. Majaron, "Monte Carlo simulation of radiation transfer in human skin with geometrically correct treatment of boundaries between different tissues," *Proc. SPIE* **8579**, 85790Z (2013).
8. T. J. Pfefer, J. K. Barton, and E. K. Chan, "A three-dimensional modular adaptable grid numerical model for light propagation during laser irradiation of skin tissue," *IEEE J. Sel. Top. Quantum Electron.* **2**, 934–942 (1996).
9. D. A. Boas et al., "Three dimensional Monte Carlo code for photon migration through complex heterogeneous media including the adult human head," *Opt. Express* **10**(3), 159–170 (2002).
10. Q. Fang and D. A. Boas, "Monte Carlo simulation of photon migration in 3D turbid media accelerated by graphics processing units," *Opt. Express* **17**(22), 20178–20190 (2009).

11. T. Binzoni, T. S. Leung, and R. Giust, "Light transport in tissue by 3D Monte Carlo: influence of boundary voxelization," *Comput. Methods Programs Biomed.* **89**(1), 14–23 (2008).
12. H. Shen and G. Wang, "A tetrahedron-based inhomogeneous Monte Carlo optical simulator," *Phys. Med. Biol.* **55**(4), 947–962 (2010).
13. H. B. Sanford et al., "The nature and evolution of port wine stains: a computer-assisted study," *J. Invest. Dermatol.* **74**(3), 154–157 (1980).

Bin Chen earned his PhD degree at Xi'an Jiaotong University, China, in 2002. He is currently a full professor and vice director at State Key Laboratory of Multiphase Flow in Power Engineering, Xi'an Jiaotong University. He has devoted his efforts to the research of photon propagation, heat transfer model, and cryogen spray cooling related to laser dermatology. Now he is serving as an editorial board member of the *Journal of Clinical Dermatology and Therapy*.

Biographies of the other authors are not available.